# Horizontal coseismic deformation of the 1999 Chi-Chi earthquake measured from SPOT satellite images: Implications for the seismic cycle along the western foothills of central Taiwan

Stéphane Dominguez, Jean-Philippe Avouac,[1,2] and Rémi Michel

Laboratoire de Détection et de Géophysique, Commissariat à l'Energie Atomique, Bruyères-le-Châtel, France

Received 6 August 2001; revised 8 April 2002; accepted 9 September 2002; published 7 February 2003.

[1] The 1999 Chi-Chi earthquake, $M_w = 7.6$, broke a major thrust fault along the western foothills of the Central Range of Taiwan. We have measured the horizontal coseismic displacement field by correlating optical satellite images acquired before and after the earthquake. These data reveal the fault trace and a clockwise rotation of surface displacements toward the north with much larger displacements and strain in the hanging wall. At the surface, coseismic slip increases from 5–6 m near the epicenter to 10–11 m to the north. In the epicentral area, we observe a left-lateral strike-slip zone trending N125°E, and farther north, a fault zone trending N-S with a right-lateral component. The data were modeled using elastic dislocations. The fault geometry consists of a shallow 20–35° east dipping ramp, which soles out into a low dipping décollement at a depth of ~6 to 8 km. Surface displacements can be satisfactorily modeled, assuming a constant slip azimuth on the main fault plane, close to the azimuth of plate convergence (N305°E ± 5°). At depth, slips along the fault plane evolve from 5–6 m in the south to 7 to 12 m to the north. Our model suggests that the deeper portion of the fault was not activated during the Chi-Chi earthquake. This zone of slip deficit must break during large earthquakes or be activated during transient episodes of aseismic slip. On the basis of these observations, the western front of the central Taiwan should produce a $M = 7$ to 7.5 event, about every 150 to 250 years. *INDEX TERMS:* 8040 Structural Geology: Remote sensing; 7209 Seismology: Earthquake dynamics and mechanics; 7230 Seismology: Seismicity and seismotectonics; 7260 Seismology: Theory and modeling; *KEYWORDS:* earthquake, Chi-Chi, Taiwan, coseismic, imagery, Okada

**Citation:** Dominguez, S., J.-P. Avouac, and R. Michel, Horizontal coseismic deformation of the 1999 Chi-Chi earthquake measured from SPOT satellite images: Implications for the seismic cycle along the western foothills of central Taiwan, *J. Geophys. Res.*, *108*(B2), 2083, doi:10.1029/2001JB000951, 2003.

## 1. Introduction

[2] On 21 September (0147 LT), 1999, a $M_w = 7.6$ magnitude earthquake occurred in the western foothills of central Taiwan, near the small town of Chi-Chi (120.89°E/23.82°N, depth of 8–10 km) [*Ma et al.*, 1999; *Kao and Chen*, 2000] (Figure 1). The focal mechanism and fault ruptures indicate thrusting on a fault striking N-S, roughly parallel to the mountain belt. This is consistent with the geodetic measurements acquired before the earthquake which indicate rapid horizontal shortening in a direction roughly perpendicular to the trend of the orogenic belt and close to the N306°E plate convergence azimuth [*Yu et al.*, 1997] (Figure 1). To date, there are only a few examples of thrust earthquakes well documented in terms of coseismic surface deformation [e.g., *Carver and McCalpin*, 1996; *Yeats et al.*, 1996; *Philip et al.*, 1992; *Philip and Meghraoui*, 1983; *King and Vita-Finzi*, 1981]. These examples show that such earthquakes produce abundant secondary features related to fold growth such as flexural slip or extrados tension cracks that may accommodate a significant fraction of the slip on the fault at depth. Coseismic slip at the surface is therefore difficult to measure and to interpret. For example, in the case of the El Asnam earthquake both seismological measurements and geodetic measurements [*Ruegg et al.*, 1982] were suggesting a slip of the order of 6 m at depth, while the fault slip measured at the surface was nowhere larger than ~3 m [*King and Vita-Finzi*, 1981; *Philip and Meghraoui*, 1983]. A strong along strike variability of the slip is also generally observed, but it is difficult to determine whether it relates to slip heterogeneity at depth or, alternatively, to lateral variation of the near-surface rupture complexity [*Carver and McCalpin*, 1996]. The Chi-Chi earthquake also produced a complex surface rupture extending over 80 km along which the fault slip was approximately estimated allowing for an only crude comparison with the geodetic measurements [*Bilham and*

[1] Also at Laboratoire de Géologie, Ecole Normale Supérieure, Paris, France.

[2] Now at Department of Geological and Planetary Sciences, California Institute of Technology, Pasadena, California, USA.


0148-0227/03/2001JB000951$09.00

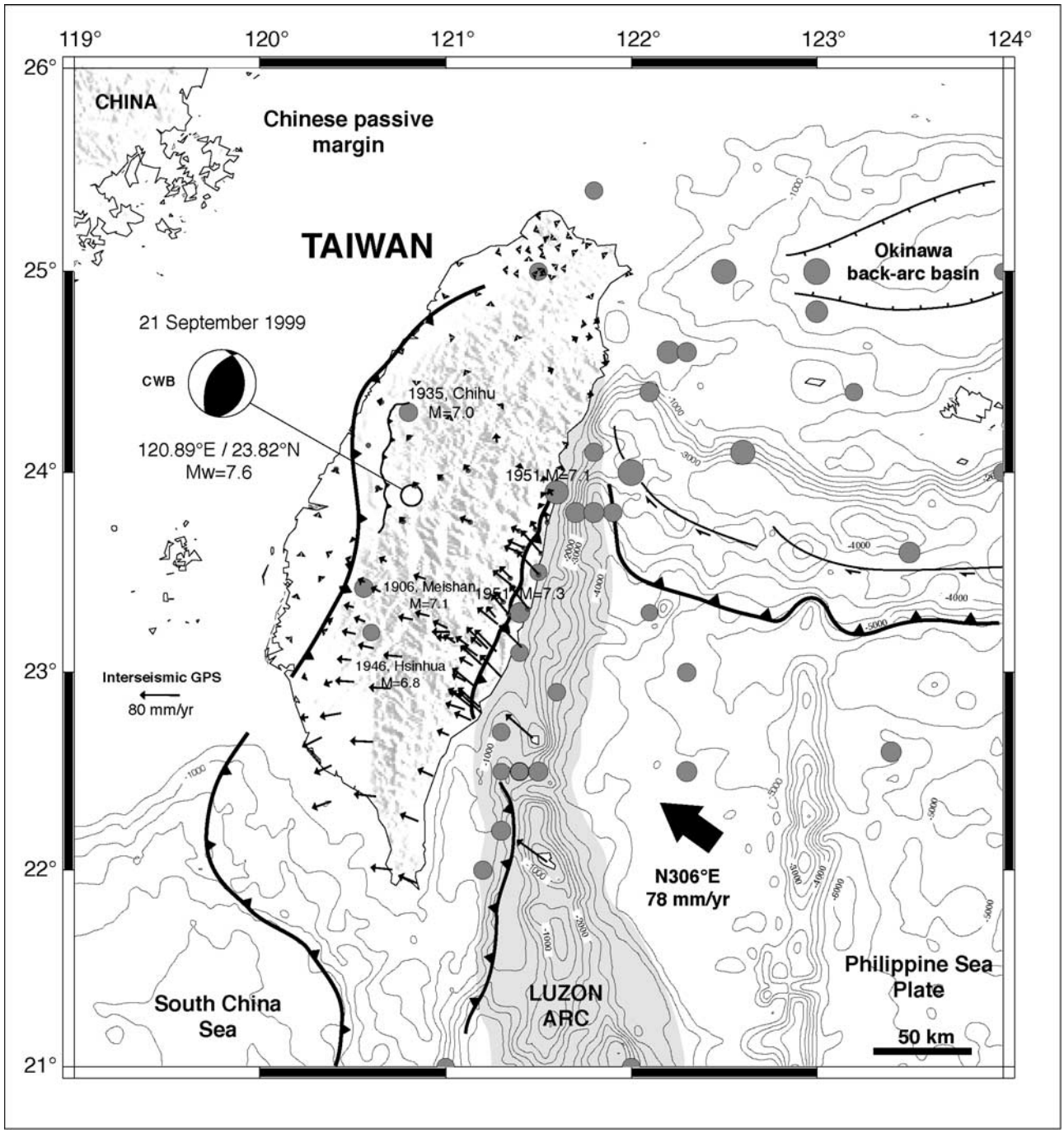


**Figure 1.** Geodynamic setting of Taiwan showing the location and focal mechanism of the Chi-Chi earthquake (CWB) and associated surface break [*Ma et al.*, 1999]. Historical seismicity from *Wang* [1998]. Thick arrow shows the motion of the Philippine Sea Plate relative to South China Block [*Seno et al.*, 1993; *Heki et al.*, 1999; *Yu et al.*, 1997]. GPS data are from *Yu et al.* [1997].

*Yu*, 2000]. Recently, it was demonstrated that coseismic surface deformation can be determined by correlating optical satellite images which seems particularly appropriate to study thrust earthquake such as the Chi-Chi event. This technique accounts for possible off-the-main-fault deformation [*van Puymbroeck et al.*, 2000; *Michel and Avouac*, 2002].

[3] Hereafter, we first provide an overview of the geological context of the Chi-Chi earthquake. We then present the technique used to measure the horizontal coseismic ground displacements from the SPOT images, and describe how these measurements were combined with the GPS data. Next, the SPOT and GPS data are used to derive an elastic model of coseismic slip that also takes into account structural constraints on the fault geometry at depth. We point to the main features of the coseismic strain field and their possible relation to the rupture process. We finally compare interseismic straining, and coseismic deformation and dis-

cuss the implications for the seismic cycle in central Taiwan.

## 2. Geological and Seismotectonic Background of the Chi-Chi Earthquake

[4] The mountain ranges of central Taiwan have formed as a result of the collision, that started less than 5 Myr ago, between the Luzon volcanic arc, carried by the Philippine Sea Plate, and the eastern margin of the South China block [*Teng*, 1990] (Figure 1). Plate convergence presently occurs at a rate of ~80 mm/yr along an azimuth close to N306°E [*Seno et al.*, 1993; *Heki et al.*, 1999; *Yu et al.*, 1997; *Miyazaki and Heki*, 2001], producing intense straining of the Taiwan island as shown by GPS geodetic measurements [*Yu et al.*, 1997, 2001; *Hu et al.*, 2001] (Figure 1). The structure of the Taiwan range has long been recognized as a crustal scale accretionary prism composed of major east dipping thrust faults [e.g., *Suppe and Jamson*, 1979; *Davis et al.*, 1983]. Active deformation is partly accommodated by thrusting along the fold-and-thrust belt that forms the western foothills of Taiwan and by strike-slip and thrust faulting along the Longitudinal Valley fault, east of Taiwan [e.g., *Suppe and Jamson*, 1979; *Angelier et al.*, 1997] (Figure 1).

[5] The epicenter of the Chi-Chi earthquake is located in the western foothills of Central Taiwan where several active thrust faults were previously identified [e.g., *Bonilla*, 1975] (Figure 2). The surface breaks follow the Chelungpu fault trace which lies east of the Taichung basin and runs N-S from Chushan to Fengyuan [e.g., *Hsu and Chang*, 1979; *Tsai*, 1995]. Surface breaks were indeed reported for ~80 km (Figure 2), with widespread evidence for reverse and left-lateral slip [*Ma et al.*, 1999; *Bilham and Yu*, 2000]. At some locations, coseismic slip observed in the field reached values as large 8–10 m [*Ma et al.*, 1999; *Bilham and Yu*, 2000]. Two others major thrust faults, the Changhua fault and the Shuantung fault, striking roughly parallel to the Chelungpu fault are considered to have been active during the Quaternary (Figure 2). The Changhua fault, which marks the front of the fold-and-thrust belt, is a blind thrust lying beneath the Pakuashan anticline. This anticline is clearly an active fault propagation fold as indicated by the deformed alluvial surfaces [*Delcaillau et al.*, 1998]. The Shuantung fault lies ~10 km east of the Chelungpu fault, and extends along strike over 50 km from Chi-Chi to Tungshih. Surface geology, seismic profiles, and well data indicate that the Chelungpu and Changhua faults cut through the Quaternary to Miocene sediment cover and root into a low dipping décollement at a depth of ~7 km [e.g., *Suppe and Jamson*, 1979; *Wang*, 2000] (Figure 2b). The shallow ramp on the Chelungpu fault dips eastward by 30° to 35° [*Suppe and Jamson*, 1979; *Hung and Suppe*, 2000] while the basal décollement is considered to dip at a shallow angle of ~6–10° beneath the eastern foothills [*Suppe and Jamson*, 1979; *Davis et al.*, 1983]. According to seismic profiles, the Chelungpu fault lies, at least in its southern part, within the Chinshui Shales, which consist of interbedded sandstone and mudstone (Figure 2b).

[6] The epicenter is located within an area where microseismic activity had been relatively quiescent in the years preceding the earthquake, the Sun Moon Lake seismic gap, except for a few events in the epicentral area which aligned approximately N120°E (see black arrow in Figure 2a). According to Harvard centroid moment tensor solution, the seismic moment, estimated to $3.38 \times 10^{20}$ N m at 120.8°E and 24.15°N, was mainly released north of the epicenter at a centroid depth of 21 km (Figure 2). Surface displacements measured from GPS [*Yu et al.*, 2001] as well as seismological records [*Ma et al.*, 2000; *Kikuchi et al.*, 2000] show that most of the slip took place north of the epicenter. If we select the eastward dipping nodal plane, the focal mechanism indicates reverse faulting along a 29° eastward dipping plane with a slight left-lateral strike-slip component. Another inversion of teleseismic waveforms [*Reymond and Okal*, 2000] yields a similar focal mechanism and moment but a shallower depth of <10 km (Figure 2). These parameters are consistent with activation of the ramp on the Chelungpu fault mainly to the north of the epicentral area [*Johnson et al.*, 2001]. As already noticed in previous case examples of shallow thrust events, near field accelerograms show a strong asymmetry in surface displacements with systematically much larger displacements on the hanging wall side of the fault trace [*Huang et al.*, 2001].

## 3. Subpixel Correlation of SPOT Images, Detection of Surface Ruptures, and Determination of Coseismic Slip

[7] Horizontal coseismic displacements can be measured from subpixel correlation of SPOT satellite panchromatic images acquired before and after the earthquake [*van Puymbroeck et al.*, 2000; *Michel and Avouac*, 2002]. In this study, we use two panchromatic SPOT images (pixel size of 10 m) (Figure 3a), which cover ~95% of the main surface break, acquired 8 months before and 2 months after the earthquake, respectively (29 January 1999 and 23 November 1999). The images have been acquired with similar near-vertical incidence (2.9° and 2.6°) in order to minimize uncertainties on the correction of topographic effects. We used a digital elevation model derived from digitization of topographic maps with a data spacing of 30 m and an uncertainty estimated to ~20 m RMS. Resulting uncertainty on topographic corrections is less than 0.1 m RMS [*van Puymbroeck et al.*, 2000].

[8] Offsets between the two images are computed from the phase shift of the Fourier transform of a sliding window [*van Puymbroeck et al.*, 2000]. Spatial sampling and the accuracy of measurements mainly depend on the local level of correlation of the images. Offsets are computed assuming that the two images differ only by a local translation that may be considered constant over a certain area represented by the sliding window. The phase shift variability at the scale of the sliding window provides an estimate of the consistency of the measurement. This variability is used to determine the coherence factor ranging from 0 (poor correlation) to 1 (perfect correlation). In the present case the coherence factor is good except above lakes and rivers, areas affected by large landslides and the regions covered by clouds (Figure 3b). After calibration, the coherence factor allows an estimate of the uncertainty on the measured offset of ~0.5 m RMS [*van*

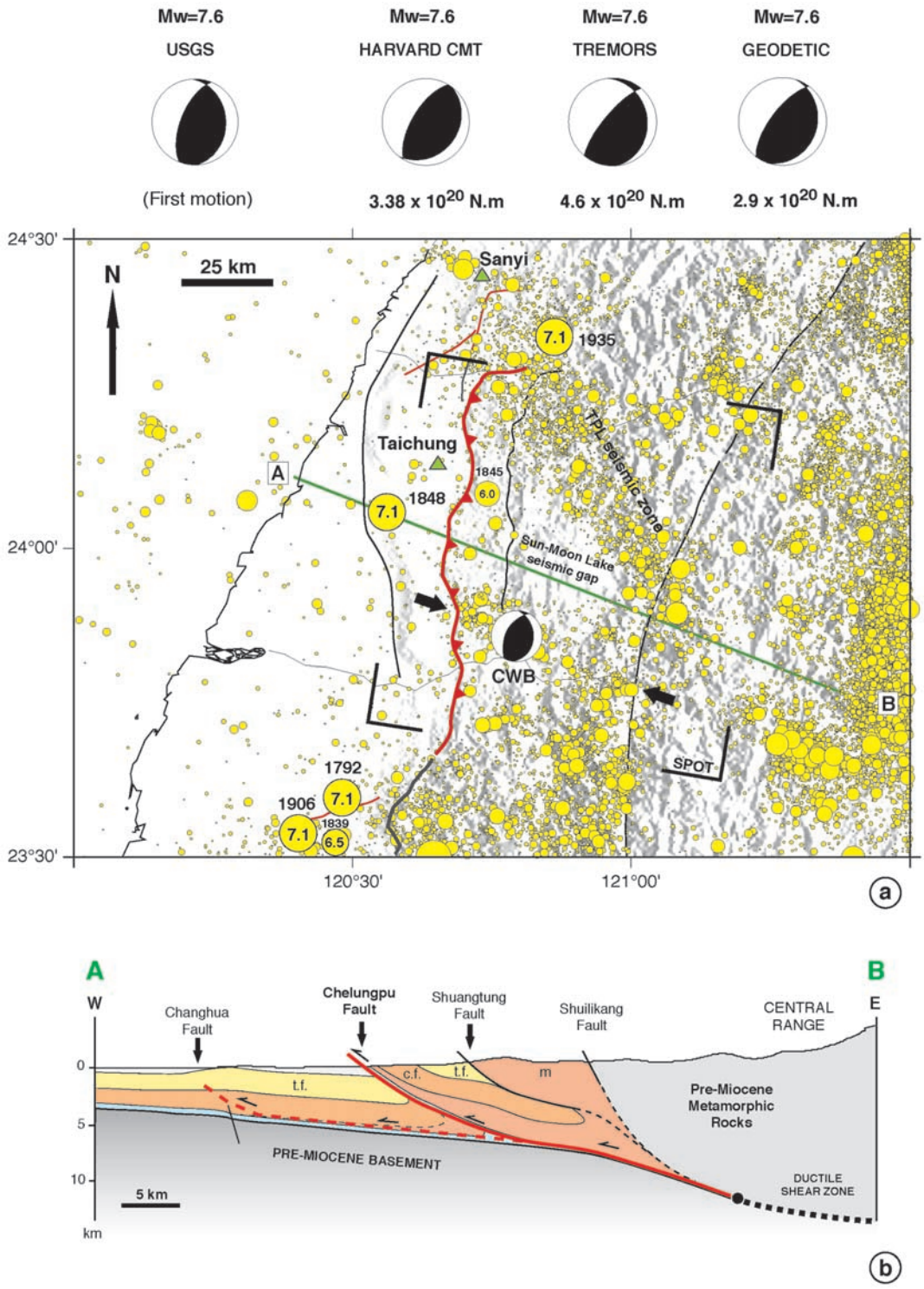


**Figure 2.** (a) Instrumental seismicity (yellow circle) recorded between 1973 and 1999 (CWB, Central Weather Bureau) and focal mechanisms of the Chi-Chi earthquake. Epicenter and focal mechanism of the 21 September main shock are after CWB. Surface breaks of the Chi-Chi earthquake are from CWB. Active faults are from Tsai and Lee (National Central University). Box shows location of the SPOT satellite images used in this study (KJ:299–302, 29 January 1999 and 23 November 1999). (b) Simplified geological cross section across the western foothills modified from *Suppe and Jamson* [1979], *Kao and Chen* [2000], and *Wang et al.* [2000]. See Figure 2a for location. The black dashed line indicates the zone of ductile shear beneath the Central Range as inferred from the GPS data on interseismic straining shown in Figure 1 [*Loevenbruck et al.*, 2001]. Red thick and dashed lines correspond to the Chelungpu and Changhua faults, respectively. Black thin lines indicate Miocene to Pleistocene sedimentary formations (m, Miocene rocks; c.f., Cholan formation; t.f., Toukoshan formation).

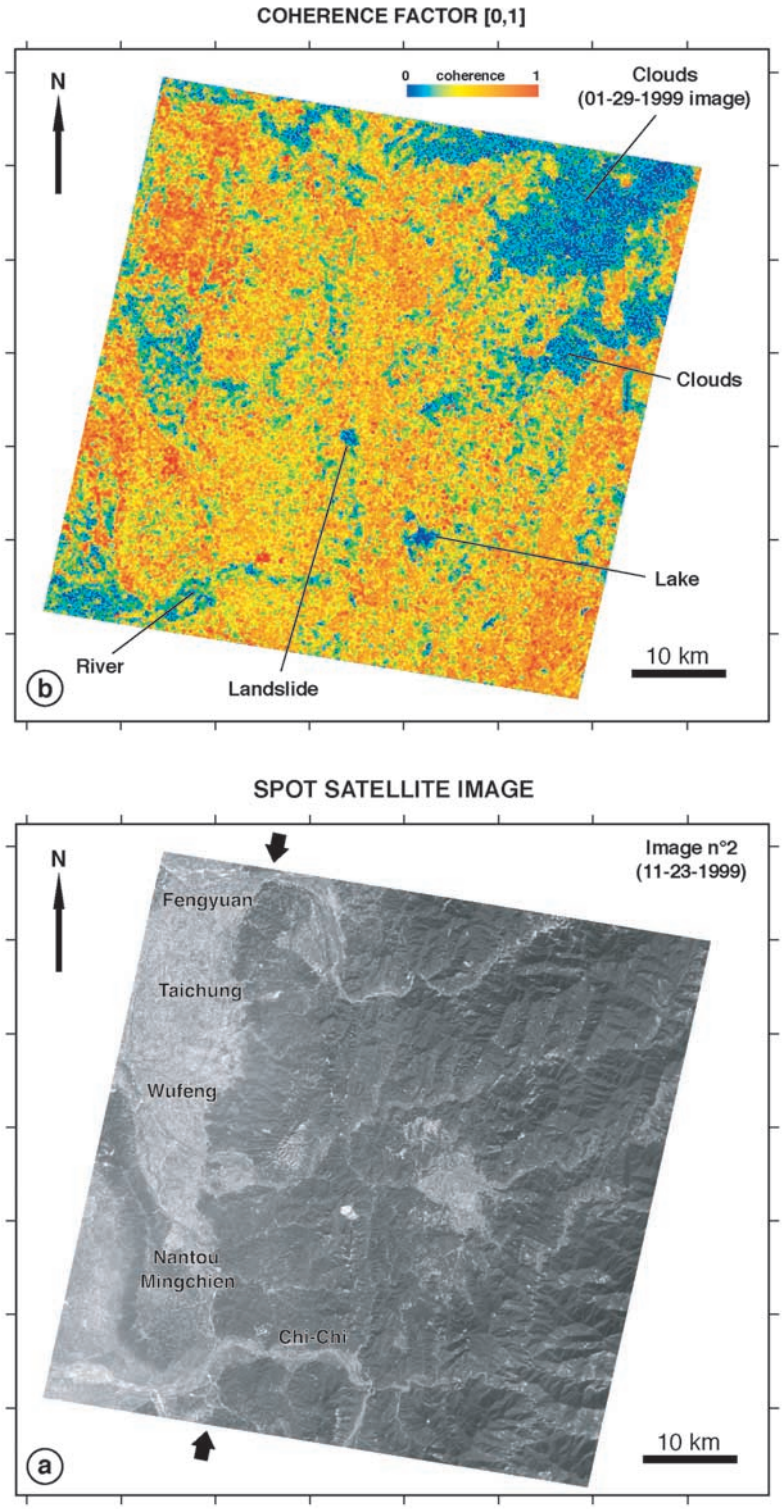


**Figure 3.** (a) SPOT satellite panchromatic image 2, acquired 2 months after the earthquake (23 November 1999). The Chelungpu Fault (black arrows) marks the boundary between the populated lowlands and the mountainous, forested hills. A major landslide triggered by the earthquake is visible near the center. (b) Coherence. The coherence depends on the degree of correlation of the two images and on the consistency of the phase shift, in the Fourier domain, with a local translation of the images [*van Puymbroeck et al.*, 2000]. The coherence is generally good, except in some limited areas due to clouds (only visible on the image 1 taken before the earthquake), landslides, or intense ground shaking in the lowlands or along the main rivers and lakes.

*Puymbroeck et al.*, 2000]. Offsets were then filtered in a multiscale procedure using a statistical determination of the correlation factor (Figure 3b). Offsets and associated uncertainties are first computed for a 16 × 16 pixels correlation window. If the uncertainty on the measured offset is larger than 0.3 pixel, the size of the correlation window is increased first to 32 × 32 pixels and then to 64 × 64 pixels if necessary. Only 5% of the measurements were filtered out by this procedure, yielding independent measurements every 160 m, in general (Figure 4). SPOT satellite images are affected by geometrical distortions because the four subarrays of detectors constituting the 6000 pixels detection line are not perfectly adjusted and because the detectors are not perfectly equally spaced. These effects induce artifacts generally smaller than 0.1 pixel (such feature can be observed in the N-S component of the offset field in Figure 4). They were estimated and compensated following the procedure described by *van Puymbroeck et al.* [2000]. The offsets in Figure 4 are also clearly affected by residual artifacts with typical >20 km wavelengths. These artifacts, which cannot be rigorously corrected from SPOT satellite orbital parameters, result from the uncertainties on the attitude (roll, pitch, and yaw) of the satellite during image acquisition [*van Puymbroeck et al.*, 2000]. Nevertheless, at this stage, the geometry of the fault rupture and the horizontal offsets along the fault can be accurately derived. On the both components (E-W and N-S), the offset field clearly reveals a strong discontinuity along the trace of the Chelungpu fault allowing detailed mapping of surface breaks with an accuracy of ∼160 m (Figures 4a and 4b). The cartography of the main surface rupture determined from SPOT satellite offsets is in very good agreement with the one derived from field observations (Figure 5b). The offset field also reveals several zones of high strain, most of which were not observed in the field or not recognized as fault ruptures (Figures 5a and 5b). These features are observed mainly east of the Chelungpu fault trace, particularly east of Nantou and east of Taichung, indicating areas of localized deformation within the hanging wall (Figures 5a and 5b).

[9] Measurements of the amplitude discontinuity at the fault on profiles trending E-W on both component of the offset field yield an accurate estimate of the horizontal component of coseismic slip, including the fault-perpendicular component which is particularly difficult to measure in the field. These measurements show a clear northward increase of both the fault-perpendicular and strike-slip components from Chushan to Taichung. North of Taichung the fault-perpendicular component decreases while the strike-slip component keeps on increasing. This results in an increase of the obliquity of coseismic slip relative to the fault strike, from ∼45° south of Taichung to ∼70° farther north. On average we measure a 4–5 m E-W component (thrust) and 5–6 m N-S component (left-lateral).

## 4. Determination of Horizontal Displacements Merging SPOT Offsets and GPS Data

[10] In the case of the Chi-Chi earthquake, 59 geodetic measurements were available in the area covered by the SPOT image [*Yu et al.*, 2001] (Figure 6). These data have been used to provide tight constraints on coseismic ground displacements at the low spatial frequencies that cannot be determined from the SPOT images. Given that no significant preseismic deformation was observed from the GPS permanent stations and that only a few cm of horizontal postseismic displacements were measured over the 3 months that followed the earthquake [*Yu et al.*, 2001], we consider that the SPOT offsets essentially represent coseismic displacements.

[11] SPOT offsets provide tight constraints on the short wavelength pattern ($\lambda < 20$ km) of the displacement field while sparse GPS data yield accurate estimate of the long wavelength ($\lambda > 20$ km). We thus merge offsets and GPS according to the following procedure. SPOT measurements were first filtered according to the signal to the coherence factor (Figure 3b) using a median filter to remove very short wavelength noise on offsets related to local temporal decorrelation induced by ground changes (coseismic landslides, changes in rivers, and lakes aspects) (Figure 6a). This process removes noise at wavelengths smaller than ∼1 km. Accurate estimate of offsets at each GPS location is computed from spatial weighted averaging to avoid residual artifacts due to geometrical distortions (see Figure 4b). Differences between offsets and GPS are next calculated for both component, E-W and N-S (Figure 6b). The residuals, which can be as large as 15 m, were then interpolated using bicubic spline functions (Figure 6b). The resulting interpolated field is filtered to remove short and medium wavelength ($\lambda < 20$ km) and then avoid local artifacts due to the heterogeneous distribution of GPS points (Figure 6b). Finally, the original offset field is compensated by removing the interpolated residual offset field (Figure 6c). This procedure gives a good correction of the displacement gradients as demonstrated by the very good correlation between the SPOT and the GPS measurements despite the fact that only the long wavelengths were modified (see details on Figure 7b). The corrected displacement field thus benefits from the dense spatial coverage provided by SPOT offsets (60 × 60 km) and the accuracy of the sparse GPS measurements (Figures 7a and 7b).

## 5. Discussion of Horizontal Coseismic Displacements

[12] Because most of the slip took place near the surface and because the fault dips shallowly eastward, the displace-

**Figure 4.** (opposite) (a) E-W and (b) N-S horizontal offsets determined from the comparison of the two SPOT images acquired 10 months before and 2 months after, respectively, the Chi-Chi earthquake. Offsets are determined from the subpixel correlation technique of *van Puymbroeck et al.* [2000], which yields independent measurements every 160 m. In some areas, shown in blacks, correlation between the two images is too low and measurements were not possible. The offset field reveals a sharp discontinuity which follows the trace of the Chelungpu fault on the SPOT image. Long-wavelength artifacts due to satellite attitude changes (roll, yaw, pitch) during image acquisition are observed locally, especially on the N-S component. Thick line gives an idea of the shape and wavelength of these artifacts.

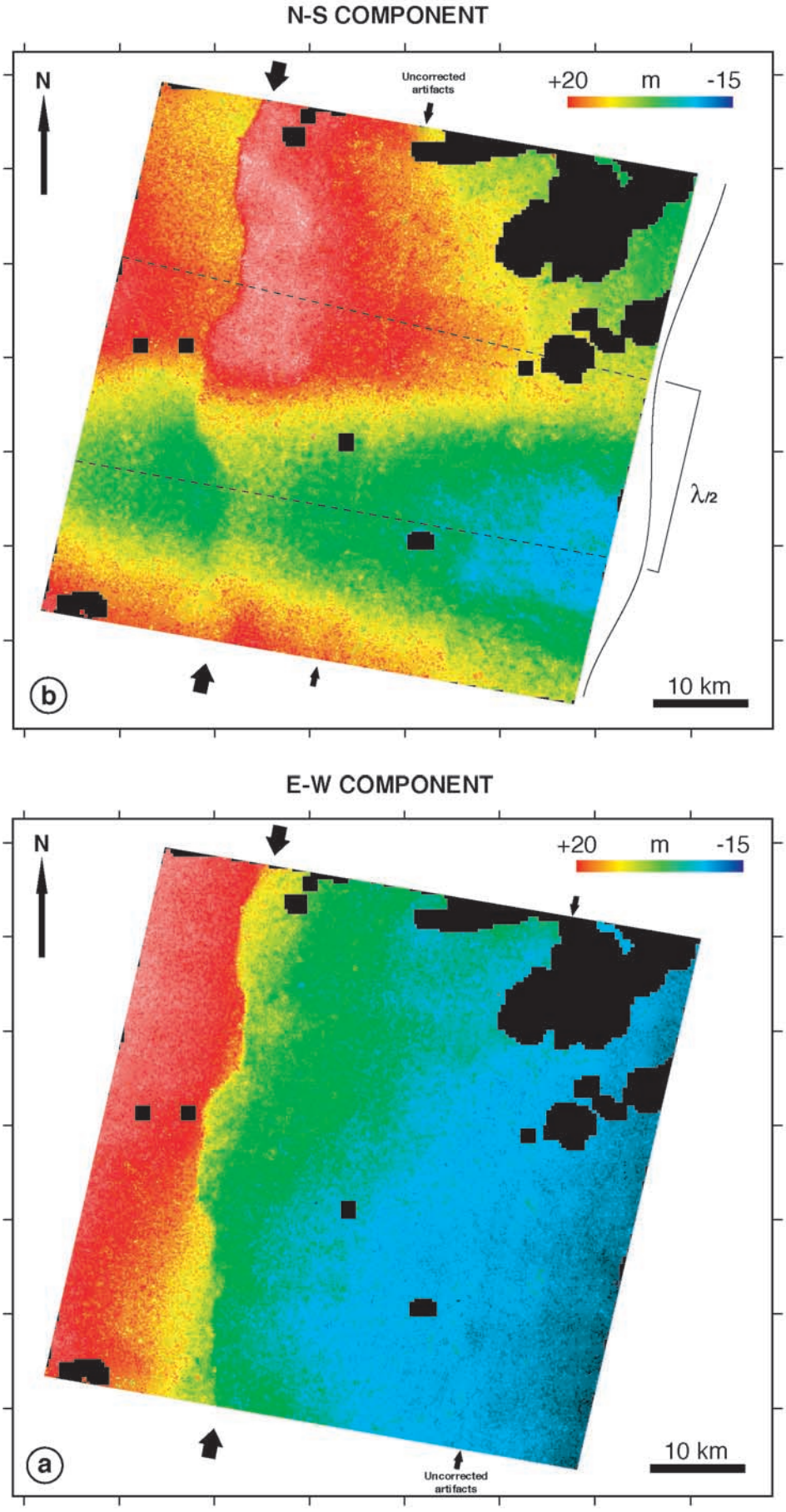
N-S COMPONENT
N
Uncorrected artifacts
+20
m
-15
λ/2
10 km
b
E-W COMPONENT
N
+20
m
-15
10 km
a
Uncorrected artifacts

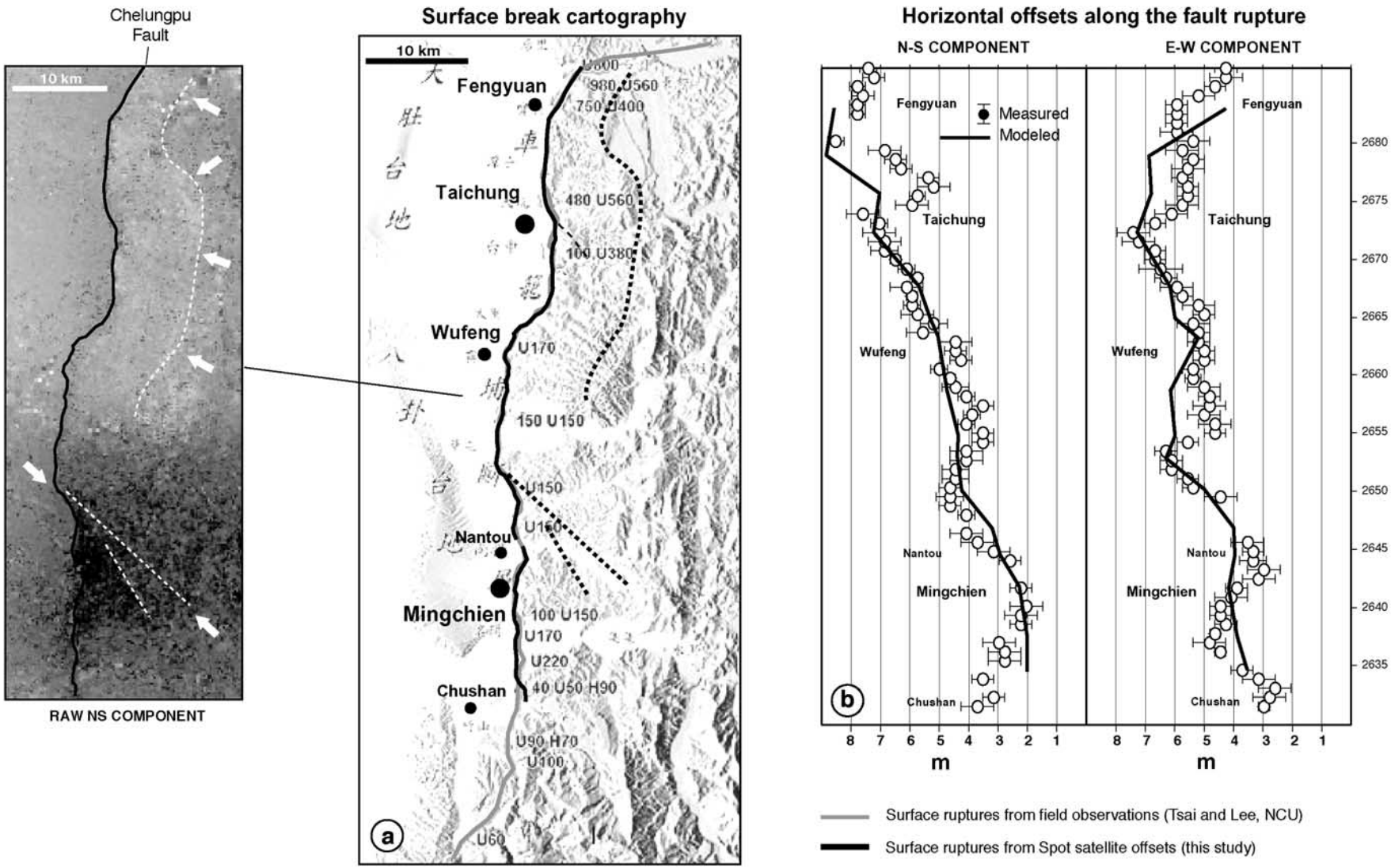


**Figure 5.** (a) Cartography of fault rupture, derived from the SPOT offset field (in light gray), compared with the fault trace measured in the field (Y. Tsai and W. H. K. Lee, National Central University) (in black). Thin dark gray lines show zones of high strain detected in the SPOT offset field. (b) E-W and N-S horizontal components of fault offset measured along the main fault trace. The measurements are made from profiles spaced every 1 km by stacking all the measurements within a 1 km wide swath. It yields independent measurements every 1 km with an accuracy close to 0.5 m. Modeled fault offsets derived from the dislocation fault model of Table 1 are shown for comparison.

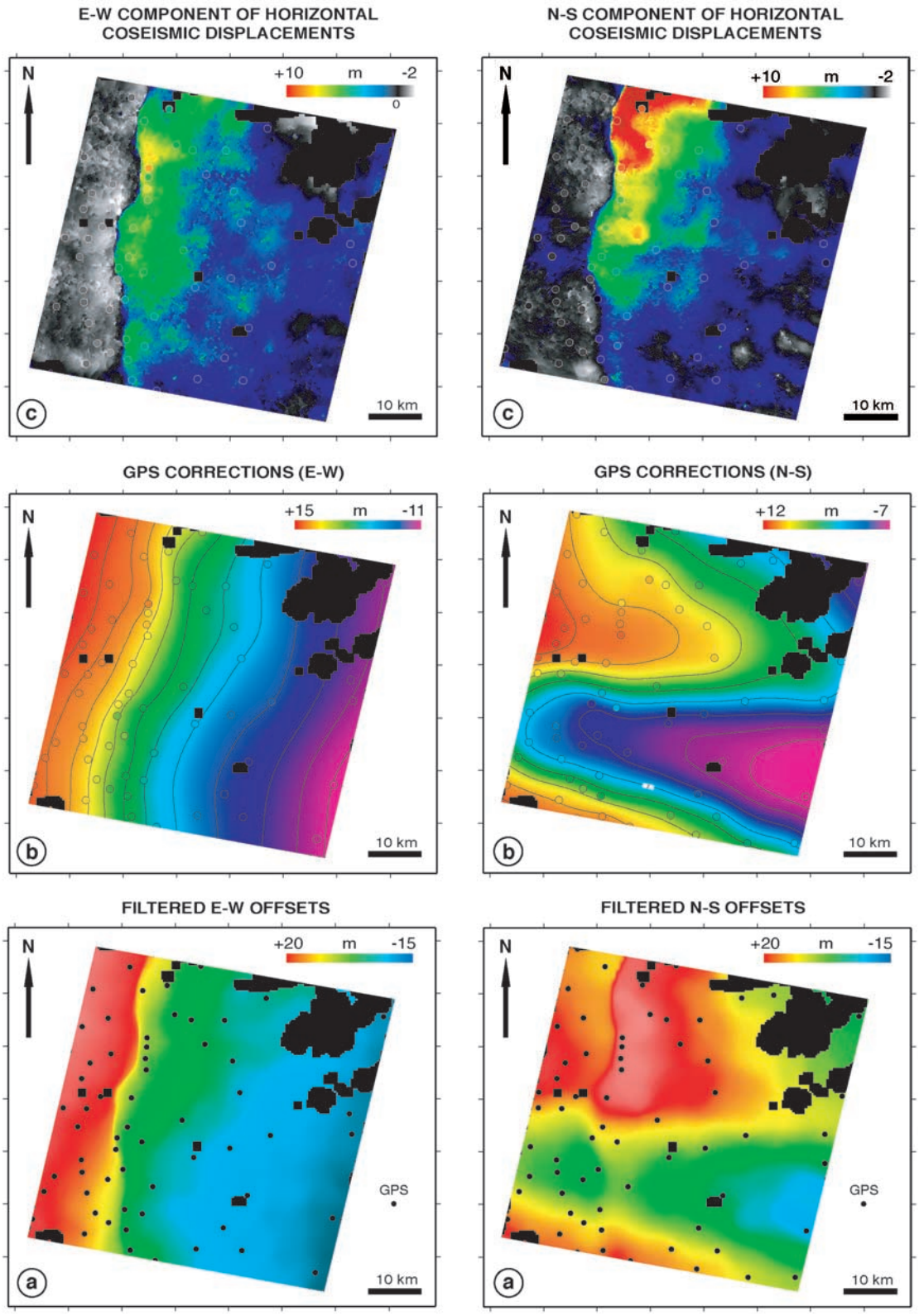


**Figure 6.** (a) E-W and N-S horizontal SPOT offsets filtered using a 16 × 16 pixels sliding window (1 pixel is 160 m). Circles show locations of the GPS measurements that were compared to the filtered offset field. (b) Residuals obtained from the comparison of the 59 GPS measurements and the SPOT offsets (circles) interpolated using bicubic spline functions (same color scale between GPS and the interpolated surface). (c) Offset field obtained after removing long-wavelength artifacts shown in Figure 6b from the initial offset field shown in Figure 3.

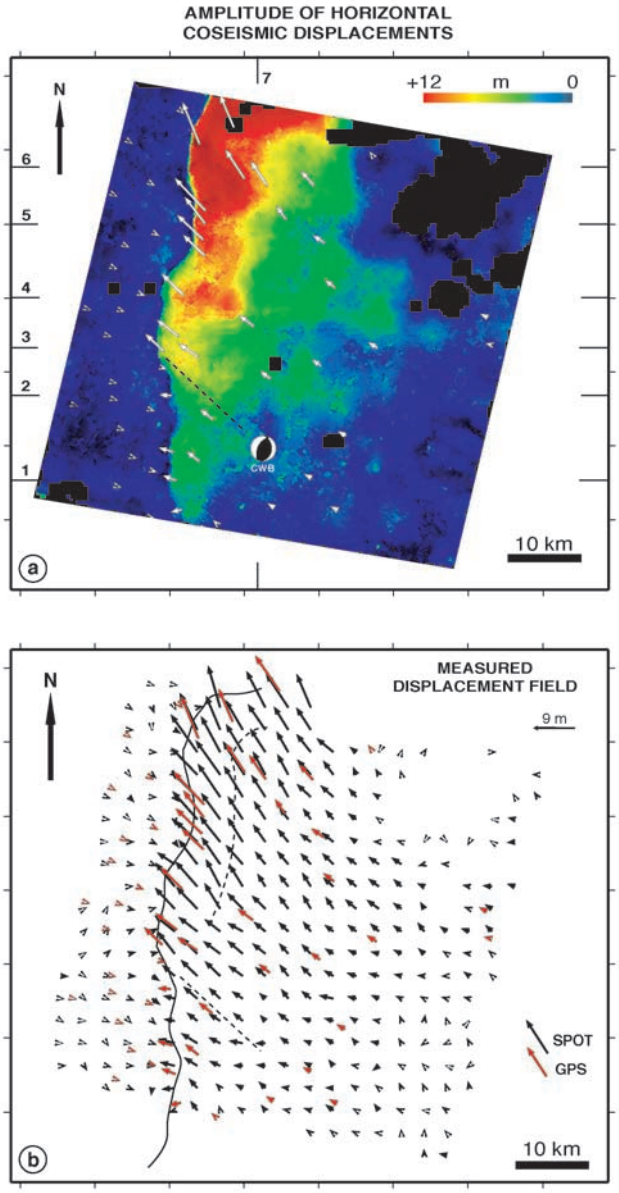


**Figure 7.** Coseismic surface displacements, (a) amplitude and (b) displacement vectors, derived from combination of GPS data and SPOT offsets. Displacements gradually increase and rotate northward to the north. Coseismic displacements measured from GPS are shown as white vectors in Figure 7a and red vectors in Figure 7b.

ment pattern at the surface provides good constraint on the slip distribution along the fault at depth.

[13] First, we observe that the large surface displacements fall within the Sun Moon Lake (SML) seismic gap as defined by instrumental seismicity recorded before the earthquake (Figures 2 and 8). If we look into more details, we observe that the southeastern part of the seismic gap is not completely filled and that large displacements are also observed somewhat beyond the SML seismic gap to the north.

[14] We note that the zone with large surface displacements is remarkably well correlated with the topographic front which defines the boundary between the western foothills and the pre-Miocene metamorphic sediments of the Central Range as well as the eastern edge of the SML (Figure 8). The Chi-Chi earthquake thus appears to have ruptured a fraction of a previously locked fault which roots below the Central Range. This situation is analogous to that along the Himalayan arc along which microseismic activity delineates the northern edge of the locked portion of the Main Himalayan Thrust fault which is also coincident with the front of the high range [*Cattin and Avouac*, 2000].

[15] Surface displacements increase north of the epicenter and their azimuths rotate clockwise (Figure 7b). Surface displacements thus tend to be more oblique to the fault to the north, as already inferred from coseismic fault slip, but we observe that the rotation is mainly concentrated within a 10–15 km zone close to the main fault trace. Farther away, coseismic displacements strike ~N300°E, in a direction close to the interseismic shortening azimuth determined from the GPS measurements [*Yu et al.*, 2001] as well as to the N306°E plate convergence azimuth across Taiwan [*Seno et al.*, 1993; *Heki*, 1999; *Miyazaki and Heki*, 2001] (Figure 1).

[16] Two main patches may actually be distinguished in the displacement field. They are separated by a zone with relatively smaller displacements that coincides with an offset along the fault trace south of Taichung. The northern patch covers an area of ~20 × 20 km$^2$ where displacements are striking N330°E with an amplitude of ~7 m on average. The southern patch covers a smaller area ~10 × 10 km$^2$ where displacements are striking N300°E with an average amplitude of 5 m. We cannot totally exclude that this pattern might result from an uncorrected artifact, but it should be noticed that it is consistent with the bimodal slip distribution deduced from the teleseismic waveforms [*Ma et al.*, 2000].

[17] Within the main patch to the north we observe a zone of high strain that runs 8–10 km east of the main fault trace between Fengyuan and Wufeng (thin red lines in Figure 5a). In this area, surface warping was observed in the field and taken to suggest blind faulting (J. Suppe personal communication, 2001). The displacement field reveals that this zone is essentially a strike-slip shear zone with ~2–3 m of right-lateral slip (Figures 5a and 6). This shear zone, which runs parallel to the main fault trace, has accommodated an opposite sense of horizontal shear which amount is as much as 25–30% of the strike-slip component along the main fault trace. As a result, the zone of northward increase in the N-S component of the displacement field appears to be confined to a limited zone of the hanging wall, lying between the main fault trace and this shear zone, which was expelled northward during the earthquake.

[18] Other tiny features are observed and might also be meaningful with regard to the rupture process. Near the epicenter of the main shock, we notice a zone with relatively sharp gradients trending N125°E (Figures 5 and 7a). The discontinuity is not as sharp as along the Chelungpu fault but suggests some left-lateral slip, of the order of 1–2 m, along a tear fault that may not have reached the surface. Several seismic events, roughly aligned along this zone, were recorded before the Chi-Chi earthquake (Figure 2). This observation suggests that the nucleation of the Chi-Chi earthquake took place near some complexity of the fault

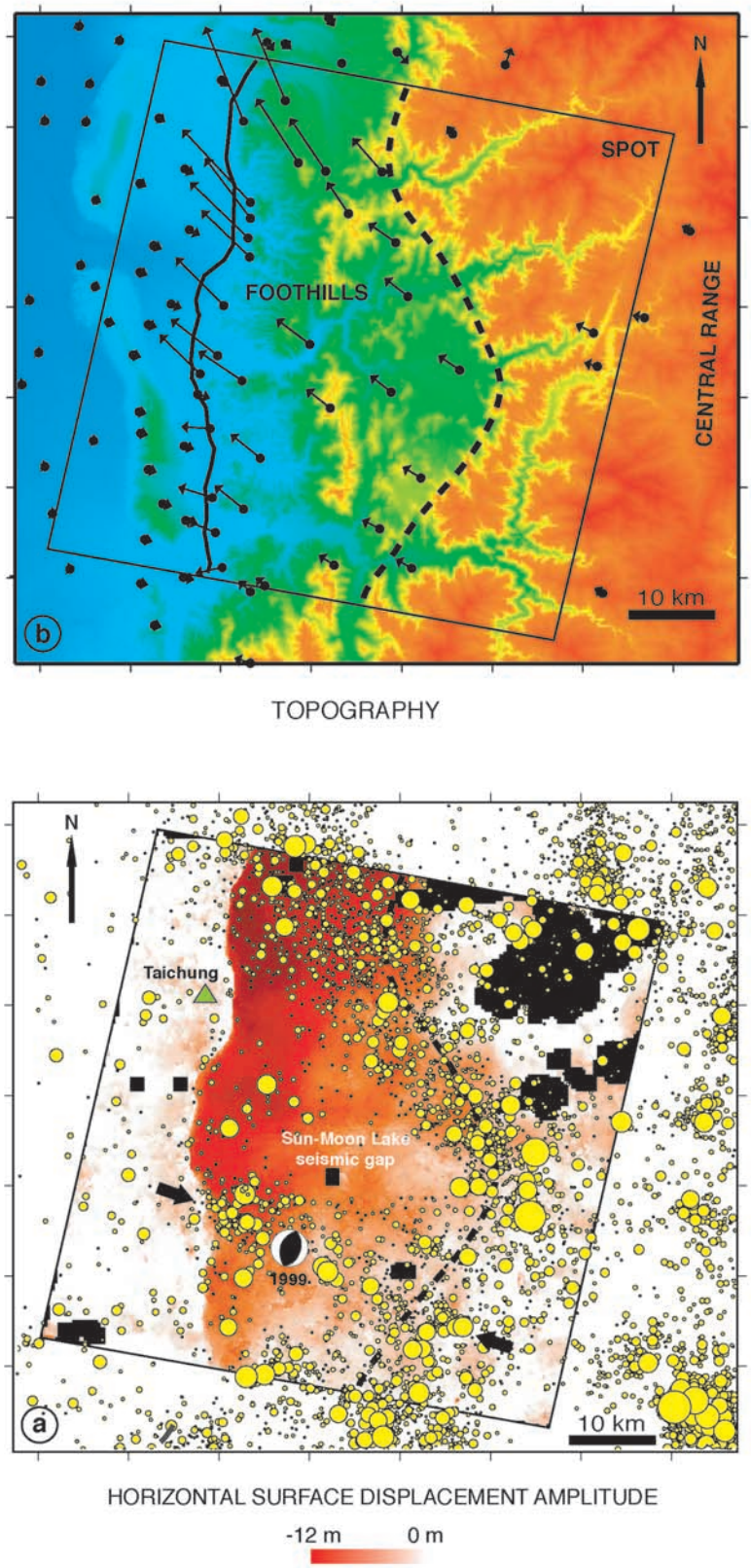


**Figure 8.** (a) Comparison of amplitude of surface displacement and the Sun Moon lake seismic gap as defined from the seismicity before the Chi-Chi earthquake. (b) The geometry of the gap and the coseismic slip distribution correlates well with the curved front of the Central Range.

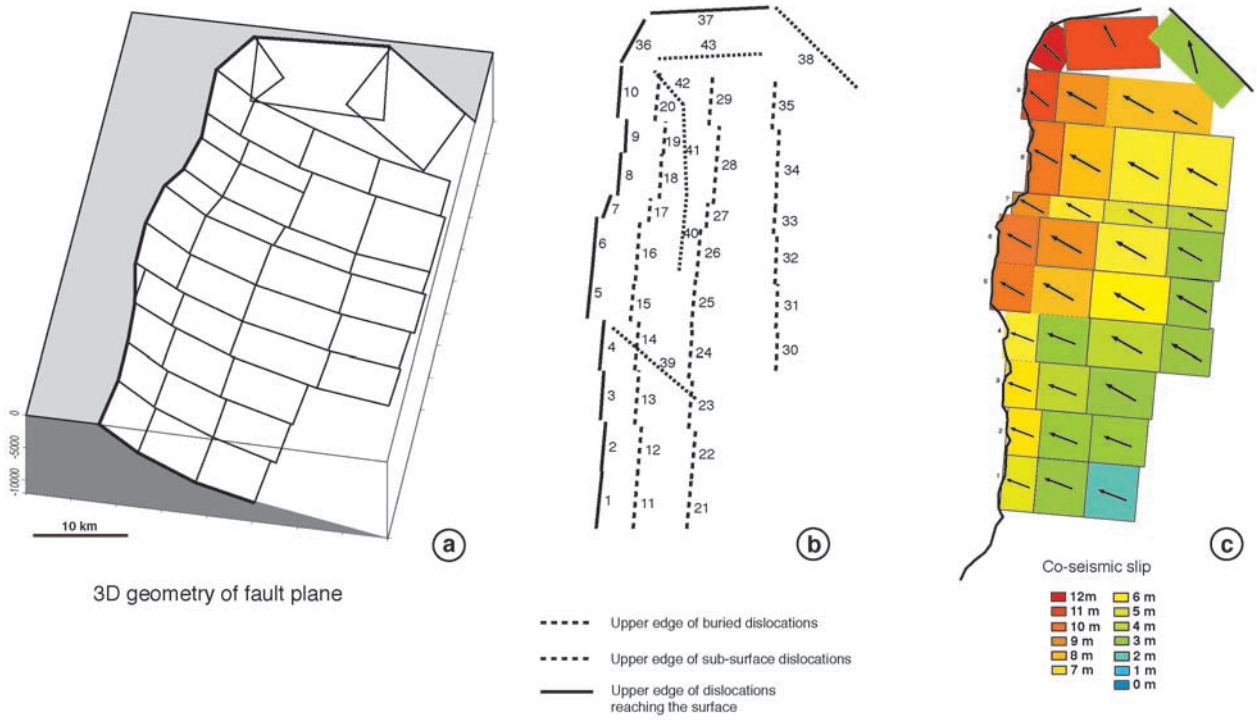


**Figure 9.** Dislocation model of the Chi-Chi earthquake coseismic surface displacements. Parameters of the fault model are given in Table 1. (a) Geometry of the main fault plane in three dimensions. (b) Location of the upper edge of each elementary dislocation in map view. (c) Map view showing slip azimuth and amplitude of slip on the 37 elementary dislocations constituting the main fault plane.

geometry related to the presence of a secondary oblique strike-slip fault.

## 6. Elastic Model of Coseismic Deformation

[19] We have modeled coseismic displacements in order to determine coseismic slip distribution along the fault plane. The modeling is based on *Okada*'s [1992] formulation for a planar dislocation in a homogeneous half-space, and computed with a 1 km grid spacing. Because a formal inversion of the data with account for structural constraints on the fault's geometry and proper account of uncertainties on GPS and SPOT offsets was beyond the scope of this study, we have adjusted the model by trial and error. The best model has been obtained after more than 350 runs, starting with only 10 dislocations while the final model consists of 43 dislocations. We estimate that slip values are constrained to better than 50 cm on the dislocations located near the fault trace (segment 1–20) and to ~1 m farther away.

[20] As a starting model, we have assumed a fault geometry derived from available balanced geological cross sections across the Chelungpu fault [*Suppe and Jamson*, 1979]. The fault model was forced to fit the observed fault trace at the surface and a 6–10° dipping décollement at 7–8 km depth (Figure 9). Moreover, following *Loevenbruck et al.* [2001], we assume that the fault must connect with a subhorizontal shear zone at a depth of ~10–12 km below the Central Range, a geometry similar to that proposed for the Himalaya of central Nepal [*Bilham et al.*, 1997; *Cattin and Avouac*, 2000]. We have assumed that the edge of this creeping zone follows the arcuate shape of the front of the range and of the seismicity belt (Figures 8 and 9). This geometry implies a midcrustal ramp connecting the creeping zone with the shallow dipping décollement.

[21] The main thrust fault was subdivided into 37 rectangular dislocations (Table 1) (Figure 9). Two additional fault segments were introduced to account for the geometry of the northern extremity of the Chelungpu fault. In this region, fault ruptures where mapped in the field (Figures 2 and 5). Additional fault segments were also added to take into account the secondary surface deformations previously described (segments 39 and 40 to 43) that are otherwise responsible for prominent local residuals.

[22] The azimuth of the slip vector on the main fault was first assumed uniform. We found the best adjustment for a slip azimuth of N305°E close to the azimuth of interseismic crustal shortening across the Central Range as indicated from GPS measurements [*Yu et al.*, 2001; *Hu et al.*, 2001]. In order to get a better fit, we found it necessary to introduce a slight clockwise rotation of slip azimuths only on the near-surface dislocations along the northern fault portion (Figure 9). We have, then, adjusted the slip and the dip angle for each dislocation by trial and error in order to match the horizontal displacement field obtained from the combination of the SPOT offsets and GPS data, as well as the horizontal and vertical components measured from GPS.

[23] It turns out that dip angles are mainly constrained from the GPS vertical components while slip amplitudes are quite tightly constrained from the horizontal displace-

**Table 1.** Dislocation Model Parameters

| No. | Length, km | Depth, km | Rake | Dip, deg | Slip, m |
|---|---|---|---|---|---|
| 1 | 5.2 | 0 | 74 | 35 | 5.0 |
| 2 | 5.2 | 0 | 74 | 35 | 6.5 |
| 3 | 5.2 | 0 | 76 | 35 | 6.5 |
| 4 | 5.2 | 0 | 71 | 35 | 6.0 |
| 5 | 6.0 | 0 | 62 | 30 | 10.0 |
| 6 | 6.0 | 0 | 60 | 30 | 10.0 |
| 7 | 5.7 | 0 | 90 | 32 | 9.0 |
| 8 | 5.2 | 0 | 63 | 30 | 9.5 |
| 9 | 5.2 | 0 | 57 | 30 | 10.0 |
| 10 | 5.2 | 0 | 57 | 35 | 11.5 |
| 11 | 7.1 | 3.0 | 60 | 25 | 2.5 |
| 12 | 7.1 | 3.0 | 60 | 25 | 3.0 |
| 13 | 7.1 | 3.0 | 60 | 25 | 4.0 |
| 14 | 7.1 | 3.0 | 60 | 25 | 2.5 |
| 15 | 8.0 | 3.0 | 60 | 22 | 7.5 |
| 16 | 8.0 | 3.0 | 60 | 22 | 9.0 |
| 17 | 7.5 | 3.0 | 60 | 23 | 7.0 |
| 18 | 7.1 | 3.0 | 60 | 25 | 7.0 |
| 19 | 7.1 | 3.0 | 60 | 25 | 7.5 |
| 20 | 7.1 | 3.0 | 60 | 25 | 9.5 |
| 21 | 6.8 | 6.0 | 60 | 17.1 | 2.0 |
| 22 | 7.4 | 6.0 | 60 | 15.7 | 2.5 |
| 23 | 8.5 | 6.0 | 60 | 13.5 | 3.0 |
| 24 | 9.6 | 6.0 | 60 | 12 | 4.0 |
| 25 | 10.0 | 6.0 | 60 | 11.4 | 5.5 |
| 26 | 9.3 | 6.0 | 60 | 13 | 5.5 |
| 27 | 8.4 | 6.0 | 60 | 15 | 4.5 |
| 28 | 7.9 | 6.0 | 60 | 18 | 6.0 |
| 29 | 7.9 | 6.0 | 60 | 20 | 7.5 |
| 30 | 7.3 | 9.0 | 60 | 7 | 2.0 |
| 31 | 7.3 | 9.0 | 60 | 7 | 2.5 |
| 32 | 8.3 | 9.0 | 60 | 7 | 3.0 |
| 33 | 8.2 | 8.0 | 60 | 10 | 3.0 |
| 34 | 8.0 | 8.6 | 60 | 13 | 3.5 |
| 35 | 8.0 | 8.6 | 60 | 15 | 4.5 |
| 36 | 5.3 | 0 | 55 | 33 | 12 |
| 37 | 8.0 | 0 | 110 | 30 | 11 |
| 38 | 12.0 | 0.5 | 120 | 45 | 3 |
| 39 | 3.0 | 0.5 | 30 | 40 | 1.5 |
| 40 | 3.0 | 0.3 | −150 | 60 | 3.5 |
| 41 | 3.0 | 0.5 | −150 | 60 | 2.5 |
| 42 | 3.0 | 0.5 | 120 | 60 | 2.0 |
| 43 | 3.0 | 0.5 | −80 | 50 | 2.5 |

ment field. The model fits nicely to the SPOT offsets, as shown from E-W profiles in Figure 10 or the scatterplot in Figure 11. The model is in agreement with the GPS horizontal components to within an RMS of 0.45 m and 0.32 m for the E-W and N-S components respectively and to the vertical component within an RMS of 0.69 m. The residuals on both GPS and SPOT offsets in Figure 12 show that the model accounts for most of the measured signal. The largest residuals are found close to the main fault trace due to the rather crude fault geometry assumed in the model. Modeled surface displacements along the fault trace are nevertheless in good agreement with the slip distribution measured from the SPOT offsets (Figures 5 and 10).

[24] The model reproduces the strong asymmetry in the observed surface displacements with much larger amplitudes on the eastern side of the fault as also deduced from the near field accelerograms [*Huang et al.*, 2001]. This effect thus appears as a simple geometric elastic effect due to the fault dip. Although slip vectors on the main fault all strike ~N305°E it also reproduces the clockwise deviation of the displacement field to the north (Figure 13). The introduction of the secondary right-lateral shear zone parallel to the main fault trace helps to reproduce this pattern and decrease residuals between model and GPS, but is not really required (Figure 12). This rotation could indeed be satisfactorily modeled by considering only a simple model of the main fault and assuming a constant slip azimuth on all the elementary dislocation (Figure 14). The clockwise rotation of the displacement field to the north thus appears to be essentially a geometric effect due to the curvature of the main fault zone to the north.

[25] The geodetic moment tensor corresponding to this model was computed from the summation of the moment tensors associated with each elementary dislocation. The resulting scalar moment of $2.9 \times 10^{20}$ N m ($M_w = 7.6$, with $\mu = 3.3 \times 10^{10}$) is close to the seismic moment of $3.38 \times 10^{20}$ N m (Harvard CMT). The geodetic moment tensor moreover corresponds to a N18°E striking fault plane, dipping 22° to the east with a 72° rake, in close agreement with the seismic moment tensor obtained from the P wave first motions or from the long-period teleseismic waveforms (Figure 2).

## 7. Discussion

[26] Our study shows that during the Chi-Chi earthquake most of the coseismic slip took place close to the surface and induced much larger strains and displacements in the hanging wall than in the footwall. This feature, which is particularly pronounced in the case of the Chi-Chi earthquake, seems to be a systematic characteristic of thrust faults often attributed to the effect of the free surface on rupture dynamics [e.g., *Brune*, 1996; *Oglesby and Archuleta*, 2000]. This effect is, in fact, purely geometric and can be reproduced by elastic modeling either of static deformation, as shown here or of the rupture kinematics [*Huang et al.*, 2001]. There is no need to advocate any particular mechanical properties of the near surface geology. We also find that the clockwise deviation of the displacement field north of the rupture zone can be reproduced by a static elastic model. It appears to be a direct effect of the curvature of the main fault to the north (which probably arises from structural control) and the obliquity of the coseismic displacements compare to the surface break direction. However, the static elastic modeling implies a coseismic strain field that is relatively at odds with the regional stress field or to long-term deformation. As discussed above, the N-S right-lateral shear zone that formed within the hanging wall, some 10 km east of the main fault trace, is clearly inconsistent with N300°E horizontal compression. This feature could reflect a zone with very weak elastic parameters (by about a factor of 10) that would have resulted in locally high coseismic elastic strain. This explanation which would require the zone of higher strains to be visible on both E-W and N-S components seems unrealistic. We rather think that this feature reflects coseismic deformation locally in excess of that needed to compensate preseismic stress. This could have resulted from a preexisting fault with a very low friction, in relation with the very large displacements on the main fault nearby.

[27] We may draw parallels with the normal faults oriented perpendicular to regional horizontal compression that are commonly observed in the hanging wall of large thrust faults. This is well documented for example along the El

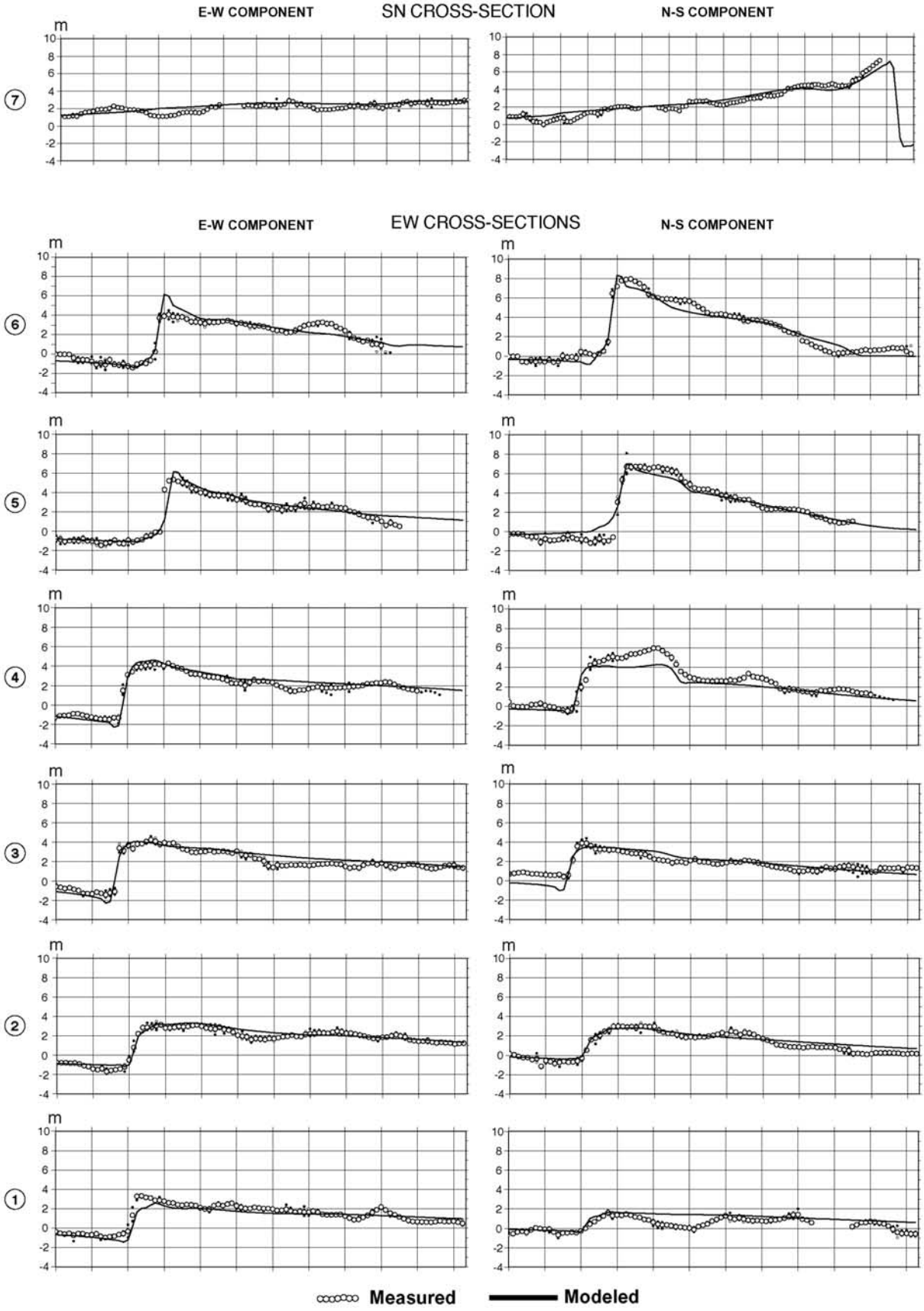


**Figure 10.** E-W Profiles showing E-W and N-S components of displacements determined from the offset field of Figure 6c (see location of the profiles on Figure 7a). Solid line shows theoretical surface displacements computed from the dislocation model in Table 1.

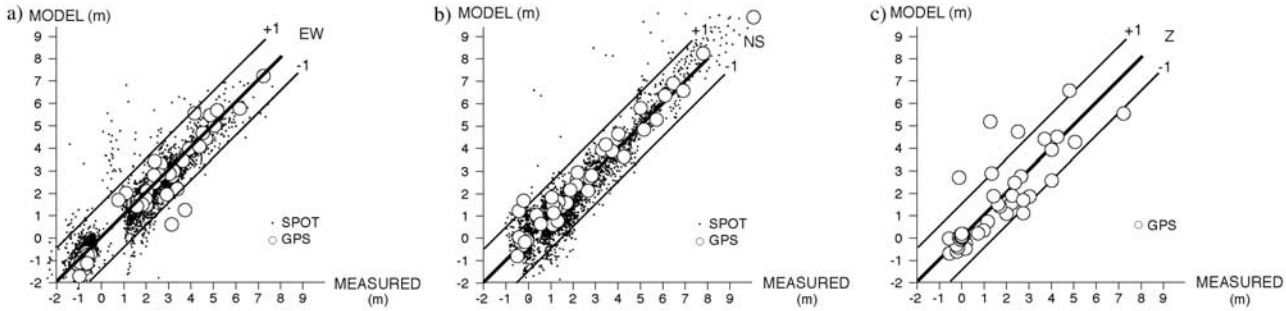


**Figure 11.** Scatterplots showing the modeled displacements compared to the observed displacements measured from the GPS and SPOT offsets. (a) E-W component, (b) N-S component, and (c) vertical component.

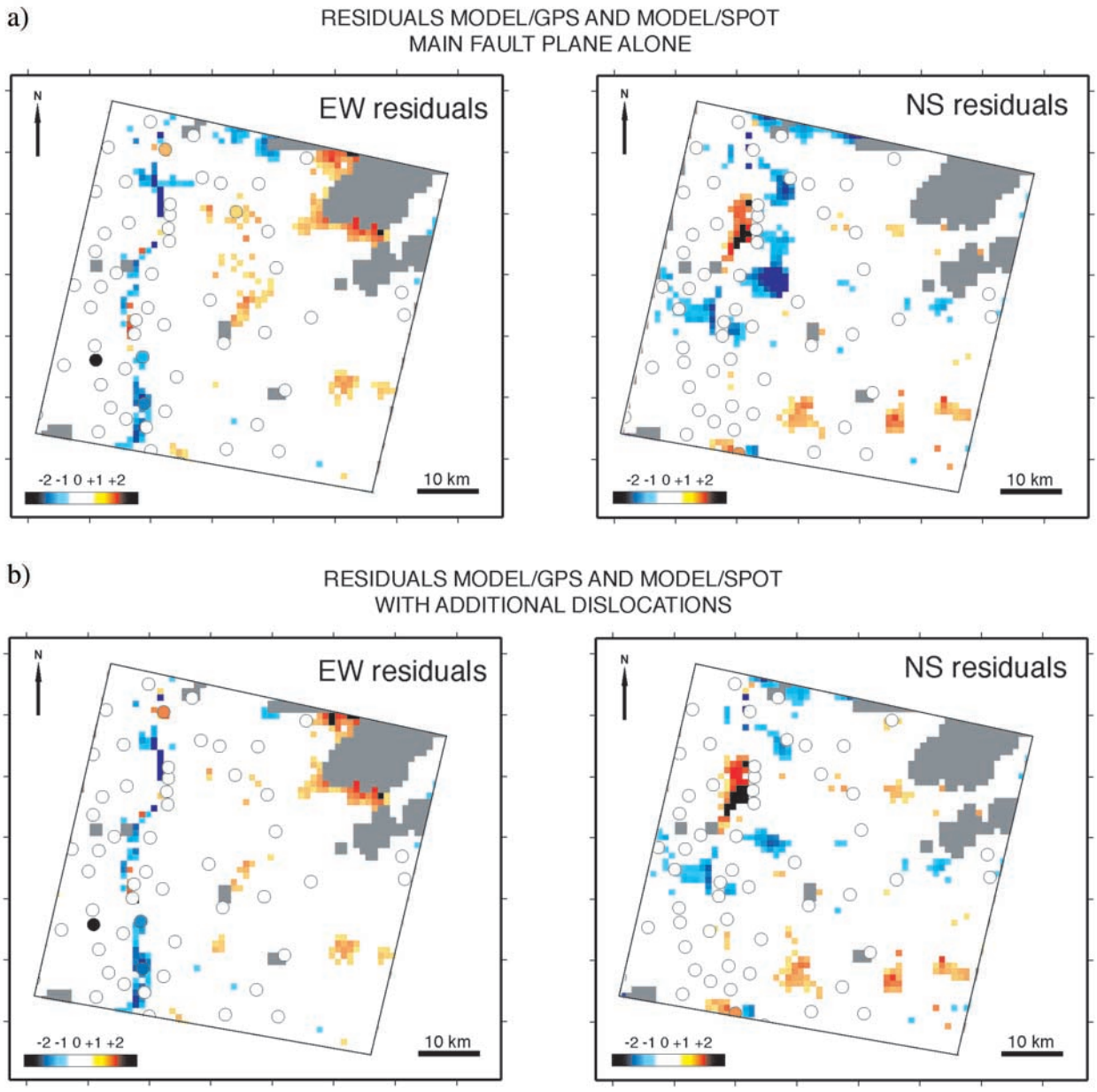


**Figure 12.** Distribution of residuals between modeled and measured horizontal displacements (map view). Circles show location of GPS data (a) using the main fault plane alone and (b) after addition of the N-S right-lateral strike-slip faults.

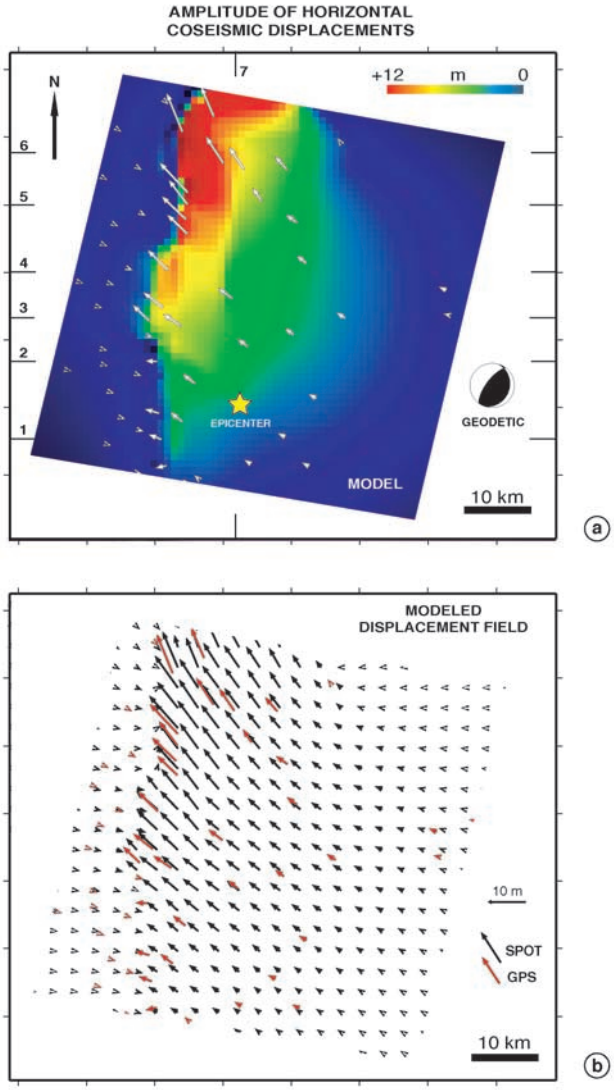


**Figure 13.** Displacement field computed from the dislocation model of Table 1. (a) Amplitudes and (b) displacement vectors. Displacement vectors computed from GPS [*Yu et al.*, 2001] are also shown for comparison. The geodetic focal mechanism is also shown.

Asnam fault [*Avouac et al.*, 1992], where the large normal faults probably reach deep and did radiate some seismic energy during the main shock [*Nabelek*, 1985].

[28] Dynamic effects probably play a key role in explaining such features. As shown by *Oglesby and Archuleta* [2000] the reduction of normal stress on the fault due to seismic waves reflected at the free surface allows a relatively large slip on the shallow dipping fault. This effect may explain why, as noticed above, the zone of large displacements extends somewhat north of the Sun Moon Lake seismic gap. The resulting large displacements at shallow depths, where deviatoric stresses are probably low, especially if preexisting faults with low friction are present in the hanging wall, can significantly alter the preseismic regional stress field.

[29] Thus our interpretation of the Chi-Chi earthquake is that the earthquake nucleated near some complexity due to the intersection with a strike-slip fault in the hanging wall that was slightly activated during the earthquake. It triggered the rupture of a large subsegment of the Chelungpu fault within the Sun Moon Lake seismic gap.

[30] Some idea of the seismic cycle along the western front of the Central Range in Taiwan can be derived by comparing coseismic deformation during the Chi-Chi earthquake, as determined from subpixel correlation of SPOT images, and interseismic strain. GPS measurements acquired before the earthquake [*Yu et al.*, 1997, 2001] clearly show that before 1999, the Central Range of Taiwan was subjected to horizontal contraction trending N300°E, (Figure 1). The observed pattern is very similar to that observed across the Himalaya of Nepal [*Bilham et al.*, 1997]. We therefore propose that, as it has been demonstrated from mechanical modeling for the Himalayan case [*Cattin and Avouac*, 2000], this pattern reflects ductile aseismic deformation along some horizontal shear zone below the range (Figure 15a). Such a process requires temperatures in excess of 350°C. The very high heat flow in the area, larger than 200 mW/m$^2$, that probably result from vertical heat advection in response to very rapid erosion at the surface suggests that such temperatures may be reached at depths of ~10 km [*Lin*, 2000] (Figure 15). We model interseismic deformation assuming subhorizontal shear at a depth of 12 km (Figure 15b). GPS data can be successfully modeled assuming a slip rate of 40 mm/yr. They moreover indicate that the westward edge of the creeping zone lies at least 40 km eastward of the trace of the Chelungpu fault, roughly beneath the steep front of the range. This means that in the period that preceded the Chi-Chi earthquake, the five segments a, b, c, d, and e were fully locked (Figure 15a). The seismicity beneath the front of the high range was probably triggered by stress build up along the edge of the ductile shear zone. Such a process also occurs in the Himalaya of Nepal where it has been well documented [*Cattin and Avouac*, 2000]. On the long term, for kinematic consistency the slip rate along segment c and d must be equal to that along the creeping zone. This slip rate is taken up by slip on the Chelungpu fault and on the Changhuah fault that reaches the Pakuashan anticline. Because the Chi-Chi earthquake only activated the shallow portion of the Chelungpu fault, the slip deficit on segment c, d and e must be compensated (Figure 15c). Because this portion of the fault clearly lies in the brittle domain we infer that it probably slips during seismic events. The slip transfer from the midcrustal shear zone to the Chelungpu fault must result from earthquakes breaking segments c, d, and e. If such an earthquake only breaks this fault width, we expect a magnitude of the order of 7 to 7.5. Another possibility is that such an earthquake would break all the way from the ductile shear zone to the near surface, a scenario analogous to that proposed for the large Himalayan earthquakes with $M_w > 8$ [*Lavé and Avouac*, 2000]. Given that the frontal thrust lying beneath the Pakuashan anticline was probably activated during a $M_s = 7.1$ event in 1948 and that the Chi-Chi earthquake is the largest know event along the Central Range, we favor the scenario in which all the faults would slip during $M_w = 7$ to $M_w = 7.6$ events with an average slip on the order of 7–8 m. In that case, we get that the western front of central Taiwan should produce an event within this range of magnitude about every 150 to 250 years which

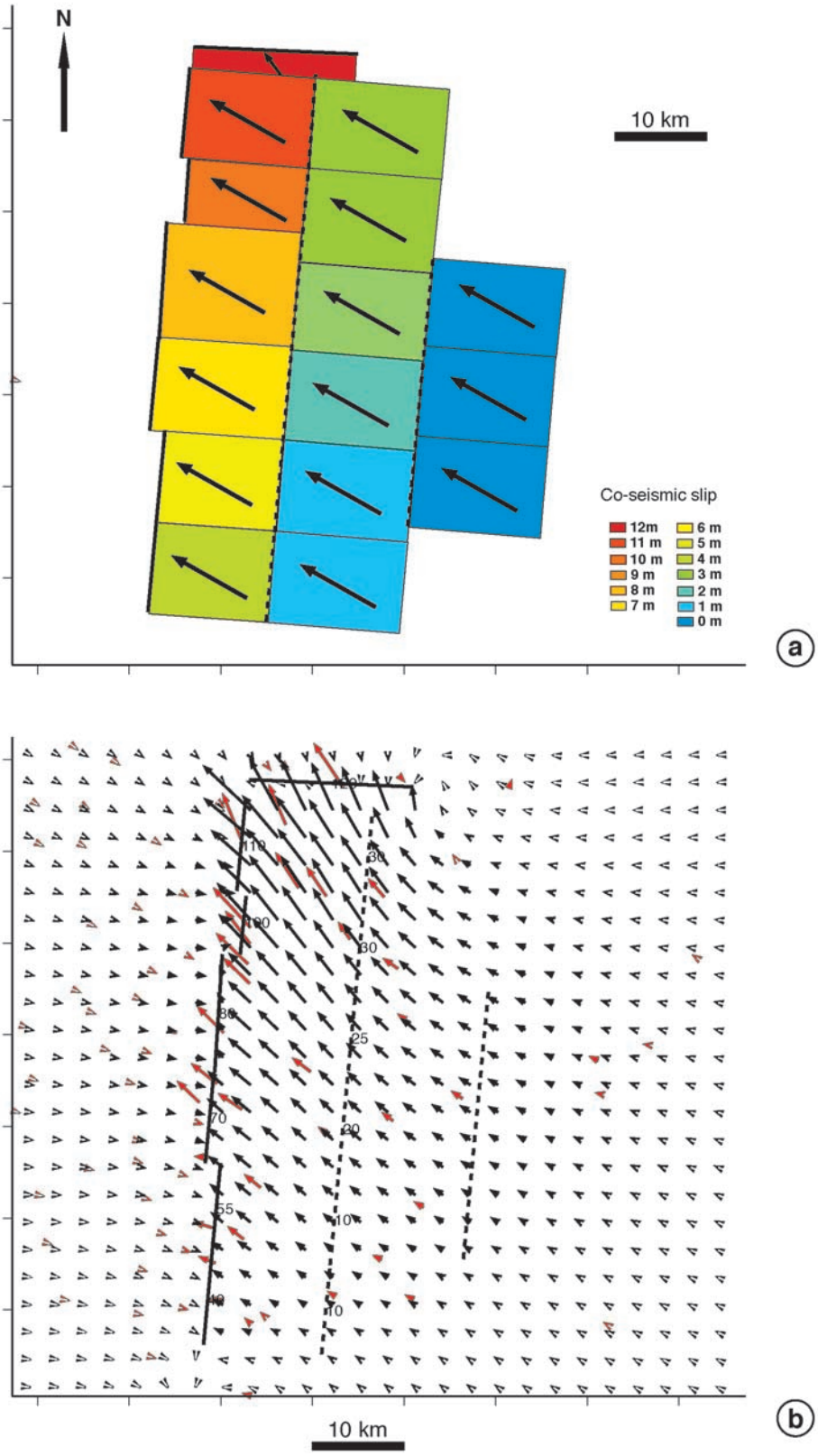


**Figure 14.** Displacement field computed considering a simplified model of the main thrust fault with a constant slip azimuth of N300°E. Thin lines show location of elementary dislocations. Note the clockwise rotation of the displacement field to the north. (a) Amplitude and azimuth of slip along each dislocations and (b) displacement vectors.

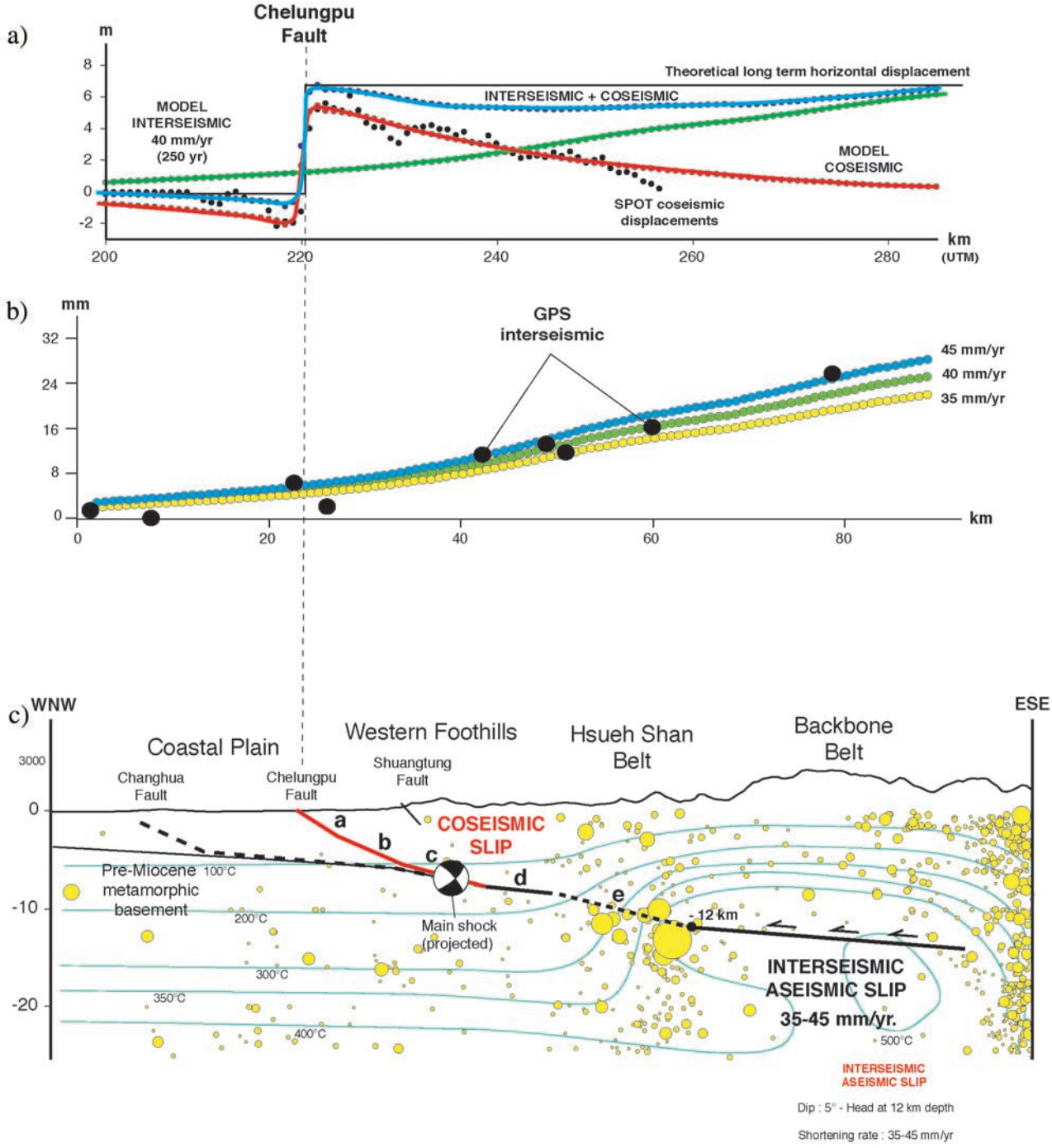


**Figure 15.** (a) Cross section of the fault model (see location on Figure 2). The geometry of the Chelungpu fault was simplified so the model matches the fault trace and meets the 6–7° east dipping décollement at 7–8 km depth. The fault probably connects with a subhorizontal shear zone below the Central Range. We also report isotherms proposed by *Lin* [2000] and seismicity recorded within a 20 km wide swath. See Figure 1 for location of section. (b) N310°E component of horizontal velocities relative to Penghu Islands within the swath shown in Figure 1. Velocities computed assuming aseismic slip along the subhorizontal shear zone. We use an elastic dislocation approximation. (c) Summation of interseismic displacements and coseismic displacements during the Chi-Chi earthquake assuming 250 years of interseismic loading.

would occur on the deep portion of the thrust fault or on the shallow portion breaking the Chelungpu fault or the Changhua fault.

[31] **Acknowledgments.** This research was funded by CEA and Ministère de la Recherche (ACI). The manuscript has benefited from comments by Gilles Peltzer, Hosuke Heki, and the associate editor Teruo Yamashita. We are also grateful to Laurent Bollinger for its help in programming the Okada dislocation model and M.-A. Gutscher for grammatical corrections of the manuscript.

## References

Angelier, J., H. T. Chu, and J. C. Lee, Shear concentration in collision zone: Kinematics of the Chihshang Fault as revealed by outcrop-scale quantification of active faulting, Longitudinal Valley, eastern Taiwan, *Tectonophysics*, *274*, 117–143, 1997.

Avouac, J. P., B. Meyer, and P. Tapponnier, On the growth of normal faults and the existence of flats and ramps along the El Asnam active fold and thrust system, *Tectonics*, *11*, 1–11, 1992.

Bilham, R., and T.-T. Yu, The morphology of thrust faulting in the 21 September 1999, Chichi, Taiwan earthquake, *J. Asian Earth Sci.*, *18*, 351–367, 2000.

Bilham, R., K. Larson, and J. Freymueller, GPS measurements of present-day convergence across the Nepal Himalaya, *Nature*, *336*, 61–64, 1997.

Bonilla, M. G., A review of recently active faults in Taiwan, *U.S. Geol. Surv. Open File Rep., 75-41*, 1975.

Brune, J., Particle motions in a physical model of shallow angle thrust faulting, *Proc. Indian Acad. Sci. Earth Planet. Sci.*, *105*, L197–L206, 1996.

Carver, A. G., and J. P. McCalpin, Paleoseismology of compressional tectonic environments, in *Paleoseismology*, edited by J. McCalpin, pp. 183–269, Academic, San Diego, Calif., 1996.

Cattin, R., and J. P. Avouac, Modeling mountain building and the seismic cycle in the Himalaya of Nepal, *J. Geophys. Res.*, *105*, 13,389–13,407, 2000.

Davis, D., J. Suppe, and F. A. Dahlen, Mechanics of fold and thrust belts and accretionary wedges, *J. Geophys. Res.*, *88*, 1153–1172, 1983.

Delcaillau, B., B. Deffontaines, L. Floissac, J. Angelier, J. Deramond, P. Souquet, H. T. Chu, and J. F. Lee, Morphotectonics in the western fold-and thrust belt of Taiwan: An integrated analysis of the Pakuashan anticline, *Geomorphology, 24*, 263–290, 1998.

Heki, K., S. Miyazaki, H. Takahashi, M. Kasahara, F. Kimata, S. Miura, N. Vasilenco, A. Ivashchenco, and K. An, The Amurian plate motion and current plate kinematics in eastern Asia, *J. Geophys. Res.*, *104*, 29,147–29,155, 1999.

Hsu, T. L., and H. C. Chang, Quaternary faulting in Taiwan, *Mem. Geol. Soc. China*, *3*, 155–165, 1979.

Hu, J. C., S. B. Yu, and J. Angelier, Active deformation of Taiwan from GPS measurements and numerical simulations, *J. Geophys. Res.*, *106*, 2265–2280, 2001.

Huang, W. G., J. H. Wang, B. S. Huang, K. C. Chen, T. M. Chang, R. D. Hwang, H. C. Chiu, and C. C. Tsai, Source parameters of the 1999 Chi-Chi, Taiwan earthquake, based on Brune's source model, *Bull. Seismol. Soc. Am.*, *91*, 1190–1198, 2001.

Hung, J.-H., and J. Suppe, Subsurface geometry of the Chelungpu fault and surface deformation style, in *Proceedings of International Workshop on Annual Commemoration of Chi-Chi Earthquake*, *September 18–20*, edited by C.-H. Loh and W.-I. Liao, pp. 133–138, Natl. Cent. for High-Performance Comput., Taipei, Taiwan, 2000.

Johnson, K. M., Y. J. Hsu, P. Segall, and S. B. Yu, Fault geometry and slip distribution of the 1999 Chi-Chi, Taiwan earthquake imaged from inversion of GPS data, *Geophys. Res. Lett.*, *28*, 2285–2288, 2001.

Kao, H., and W.-P. Chen, The Chi-Chi earthquake sequence: Active out-of-sequence thrust faulting in Taiwan, *Science*, *288*, 2346–2349, 2000.

Kikuchi, M., Y. Yagi, and Y. Yamanaka, Source process of the Chi-Chi Taiwan earthquake of September 21, 1999 inferred from teleseismic body waves, *Bull. Earthquake Res. Inst. Univ. Tokyo*, *75*, 1–13, 2000.

King, G. C. P., and C. Vita-Finzi, Active folding in the Algerian earthquake of 10 October 1980, *Nature*, *292*, 22–26, 1981.

Lavé, J., and J. P. Avouac, Active folding of fluvial terraces across the Siwalik Hills (Himalaya of central Nepal), *J. Geophys. Res.*, *105*, 5735–5770, 2000.

Lin, C.-H., Thermal modeling of continental subduction and exhumation constrained by heat flow and seismicity in Taiwan, *Tectonophysics*, *324*, 189–201, 2000.

Loevenbruck, A., R. Cattin, and X. Le Pichon, Elastic deformation and seismic cycle in Taiwan derived from GPS measurements, *C. R. Acad. Sci., Ser. I*, *333*, 57–64, 2001.

Ma, H. F., C. T. Lee, Y. B. Tsai, T. C. Shin, and J. Mori, The Chi-Chi, Taiwan earthquake: Large surface displacements on an inland thrust fault, *Eos Trans. AGU*, *80*(50), 605–611, 1999.

Ma, H.-F., T.-R. A. Song, S.-J. Lee, and H. I. Wu, Spatial slip distribution of the September 20, 1999, Chi-Chi, Taiwan, earthquake (*Mw* 7.6)—Inverted from teleseismic data, *Geophys. Res. Lett.*, *27*, 3417–3420, 2000.

Michel, R., and J. P. Avouac, Deformation due to the 17 August 1999 Izmit earthquake measured from SPOT images, *J. Geophys. Res.*, *107*(B4), 2062, doi:10.1029/2000JB000102, 2002.

Miyazaki, S., and K. Heki, Crustal velocity field of southwest Japan: Subduction and arc-arc collision, *J. Geophys. Res.*, *106*, 4305–4326, 2001.

Nabelek, J., Geometry and mechanism of faulting of the 1980 El Asnam, Algeria, earthquake from inversion of teleseismic body waves and comparison with field observations, *J. Geophys. Res.*, *90*, 12,713–12,728, 1985.

Oglesby, D. D., and R. J. Archuleta, Dynamics of dip-slip faulting: Exploration in two dimensions, *J. Geophys. Res.*, *105*, 13,643–13,653, 2000.

Okada, Y., Internal deformation due to shear and tensile faults in a half-space, *Bull. Seismol. Soc. Am.*, *82*, 1018–1040, 1992.

Philip, H., and M. Meghraoui, Structural analysis and interpretation of the surface deformation of the El Asnam earthquake of October 10, 1980, *Tectonics*, *2*, 17–49, 1983.

Philip, H., E. Rogozhin, A. Cisternas, J. C. Bousquet, B. Borisov, and A. Karakhanian, The Armenian earthquake of December 7: Faulting and folding, neotectonics and paleoseismicity, *Geophys. J. Int.*, *110*, 141–158, 1992.

Reymond, D., and E. A. Okal, Preliminary determination of focal mechanisms from the inversion of spectral amplitudes of mantle waves, *Phys. Earth Planet. Inter.*, *121*, 249–271, 2000.

Ruegg, J. C., M. Kasser, A. Tarantola, J. C. Lepine, and B. Chouikrat, Deformations associated with the El Asnam earthquake of 10 October 1980: Geodetic determination of vertical and horizontal movements, *Bull. Seismol. Soc. Am.*, *72*, 2224–2227, 1982.

Seno, T., S. Stein, and A. E. Gripp, A model for the motion of the Philippine Sea Plate consistent with NUVEL-1 and geological data, *J. Geophys. Res.*, *98*, 17,941–17,948, 1993.

Suppe, J., and J. Jamson, Fault-bend origin of frontal folds of the western Taiwan fold-and-thrust belt, *Petrol. Geol. Taiwan*, *16*, 1–18, 1979.

Teng, L., Geotectonic evolution of late Cenozoic arc-continental collision in Taiwan, *Tectonophysics*, *183*, 57–76, 1990.

Tsai, Y. B., A study of disastrous earthquakes in Taiwan, 1683–1895, *Bull. Inst. Earth Seismol. Acad. Sin.*, *5*, 1–44, 1995.

van Puymbroeck, N., R. Michel, R. Binet, J.-P. Avouac, and J. Taboury, Measuring earthquakes from optical satellite images, *Appl. Opt.*, *39*(20), 3486–3494, 2000.

Wang, C.-Y., C.-H. Chang, and H.-Y. Yen, An interpretation of the 1999 Chi-Chi earthquake in Taiwan based on the thin-skinned thrust model, *TAO*, *11*(3), 609–630, 2000.

Wang, J. H., Studies of earthquake seismology in Taiwan during the 1897–1996 period, *J. Geol. Soc. China*, *14*(3), 291–336, 1998.

Yeats, R., K. Sieh, and C. R. Allen, *The Geology of Earthquake*, 568 pp., Oxford Univ. Press, New York, 1996.

Yu, S. B., H. Y. Chen, and L. C. Kuo, Velocity field of GPS stations in the Taiwan area, *Tectonophysics*, *274*, 41–59, 1997.

Yu, S. B., et al., Preseismic deformation and coseismic displacements associated with the 1999 Chi-Chi, Taiwan earthquake, *Bull. Seismol. Soc. Am.*, *91*, 995–1012, 2001.

S. Dominguez and R. Michel, Laboratoire de Détection et de Géophysique, Commissariat à l'Energie Atomique, F-91680 Bruyères-le-Châtel, France. (dominguez@dstu.univ-montp2.fr)

J.-P. Avouac, Department of Geological and Planetary Sciences, California Institute of Technology, Mail code 100-23, Pasadena, CA 91125, USA. (avouac@gps.caltech.edu)